Quantum Phenomena Emerging Near a Ferroelectric Critical Point in a Donor–Acceptor Organic Charge-Transfer Complex

Fumitaka Kagawa [1,*], Sachio Horiuchi [2] and Yoshinori Tokura [1,3]

[1]   RIKEN Center for Emergent Matter Science (CEMS), Wako 351-0198, Japan; tokura@riken.jp
[2]   Flexible Electronics Research Center, National Institute of Advanced Industrial Science and Technology (AIST), Tsukuba, Ibaraki 305-8565, Japan; s-horiuchi@aist.go.jp
[3]   Department of Applied Physics, The University of Tokyo, Tokyo 113-8656, Japan
[*]   Correspondence: fumitaka.kagawa@riken.jp

Abstract: When a second-order transition point is decreased to zero temperature, a continuous quantum phase transition between different ground states is realized at a quantum critical point (QCP). A recently synthesized organic charge-transfer complex, TTF-2,5-QBr_2I_2, provides a platform for the exploration of the quantum phenomena that accompany a ferroelectric QCP. Here, we summarize the recent results showing the quantum phenomena associated with the ferroelectric QCP in TTF-2,5-QBr_2I_2. Whereas the enhanced quantum fluctuations lead to quantitative changes in the critical exponents of the critical phenomena, they qualitatively change the nature of the domain-wall kinetics from thermally activated motion to temperature-independent tunneling motion. The present findings highlight the great influence of quantum fluctuations on the low-temperature physical properties and suggest that TTF-2,5-QBr_2I_2 is a model system for the uniaxial ferroelectric QCP.

Keywords: quantum criticality; ferroelectric; neutral-ionic transition; organic charge-transfer complex; domain-wall dynamics

---

1. Introduction

A continuous phase transition or second-order phase transition is frequently observed in charge, spin, orbital and lattice degrees of freedom in matter. Near a transition point, the thermally driven fluctuations of order parameter become strongly enhanced, leading to a phase transition in a continuous manner: this behavior is referred to as classical critical phenomena. The second-order transition temperature or critical point can often be systematically decreased, for instance, by using pressure, a magnetic field, or chemical doping. When the critical point of the second-order transition eventually reaches zero temperature, an intriguing zero-temperature continuous transition emerges between the ground states of the system. Obviously, thermally driven order-parameter fluctuations cannot be involved in such a zero-temperature transition, so some diverging fluctuations that are supposed to accompany a continuous transition are expected to arise via a quantum-mechanical origin. This issue, referred to as quantum criticality, is one of the most important problems in contemporary condensed matter physics [1–4].

A growing number of extensive studies on quantum criticality are revealing that although matter can never be cooled to a zero-temperature critical point or quantum critical point (QCP), the physical properties at finite temperatures can be strongly affected by the presence of a QCP, as evidenced by the unconventional temperature dependence of specific heat [5], resistivity [6], and other properties: These behaviors appear to be not readily accounted for within the framework of classical critical

phenomena and Fermi-liquid theory. More remarkably, especially in itinerant systems, exotic forms of quantum order, such as superconductivity, often emerge in the vicinity of a QCP [7,8]. The enhanced quantum criticality therefore appears to have a great impact on the high density of gapless electron-hole excitations on the Fermi surface [9]. Conversely, the true divergence of quantum criticality toward a QCP is often avoided by the emergence of a new stable phase of matter.

Recently, physical properties around a ferroelectric QCP have been extensively studied, and it has been revealed that the nature of quantum criticality in ferroelectrics is remarkably different from that in itinerant ferromagnets [10–16]: In the case of itinerant ferromagnetic systems, it has been theoretically predicted that the existence of high-density gapless particle-hole excitations transforms the second-order transition at high temperatures into a discontinuous first-order transition at the lowest temperature, thereby interrupting the divergence of the quantum criticality [17]; moreover, as mentioned above, emergent new quantum orders often mask the QCP [7,8,18,19]. By contrast, in the case of insulating ferroelectrics, such instabilities are naturally avoided because of the absence of the Fermi surface, and therefore, insulating ferroelectrics provide a unique platform in the field of quantum phase transitions.

In this article, we highlight our recent progress in the study of quantum phenomena associated with the ferroelectric QCP, with a particular focus on the organic charge-transfer complex TTF-2,5-QBr$_2$I$_2$ [20,21]. In contrast to DMTTF-2,6-QBr$_{4-n}$Cl$_n$, which is located near an antiferroelectric QCP [22], TTF-2,5-QBr$_2$I$_2$ exhibits a ferroelectric QCP under a moderate pressure of 0.25–0.26 GPa, which thus facilitates experimental characterizations of order-parameter-related quantities such as spontaneous electric polarization and permittivity with the pressure as a control parameter for the quantum phase transition. We show that quantum fluctuations developing toward the QCP affect not only the thermodynamic properties, such as the critical phenomena, but also non-equilibrium properties, such as electric-field-driven creep motion of ferroelectric domain walls. Whereas the enhanced quantum fluctuations lead to quantitative changes in the critical exponents of the critical phenomena regarding the dielectric quantities, they qualitatively change the nature of the domain-wall kinetics from thermally activated motion to temperature-independent tunneling motion.

2. Crystal Structures

The crystal structures of the organic charge-transfer complexes that will be discussed in this article all consist of alternate stackings of a donor molecule, such as TTF (tetrathiafulvalene) or DMTTF (4,4′-dimethyltetrathiafulvalene), and an acceptor molecule, such as QCl$_4$, 2,6-QBr$_2$Cl$_2$ or 2,5-QBr$_2$I$_2$ (halogen-substituted quinone) (Figure 1a). At high temperatures, the donor and acceptor molecules stack with a uniform spacing, and thus, each stack preserves centrosymmetry; that is, each stack is non-polar and has no electric dipole (Figure 1b). At low temperatures, by contrast, the mixed stack is prone to (but does not always) forming a donor–acceptor dimerized stack because of an instability inherent to quasi-one-dimensional systems [23–26]. The dimerized stack obviously breaks centrosymmetry and thus hosts an electric dipole (Figure 1c). Nevertheless, the relative direction of the polarity among different stacks is another issue to be considered: upon the dimerization of the donor (D) and acceptor (A) molecules, two dimerization patterns, DA DA ⋯ and AD AD ⋯, are possible, where the underline denotes a dimerized pair. Thus, depending on the relative dimerization pattern between the neighboring stacks, the dimerized organic charge-transfer complexes can be either ferroelectric, as in TTF-QCl$_4$ [27,28] and TTF-QBr$_4$ [26,29,30], or antiferroelectric, as in DMTTF-QCl$_4$ [22].

Furthermore, the dimerization in the mixed-stack systems is often accompanied by a sizeable increase in the valence or ionicity of the donor and acceptor molecules, so TTF-QCl$_4$ and DMTTF-QCl$_4$ are also referred to as a neutral-ionic transition system [22,27]. Because a smaller lattice constant acquires a larger gain of Madelung energy in an ionic phase, the application of physical or chemical pressures tends to increase the transition temperature of a dimerized ionic phase [31]. In fact, although some materials, such as DMTTF-QBr$_4$ [22] and TTF-QI$_4$ [20,32], exhibit no dimerization down to the lowest temperature at ambient pressure, the ionic dimerized phase appears upon the application

of physical or chemical pressures. Chemical pressure can be achieved by partially substituting the halogen atoms in the quinone with smaller atoms; for instance, non-substituted DMTTF-QBr$_4$ under pressure exhibits physical properties parallel to those of Cl-substituted DMTTF-QBr$_{4-n}$Cl$_n$ at ambient pressure, suggesting that halogen substitution is approximately equivalent to a pressure change [22].
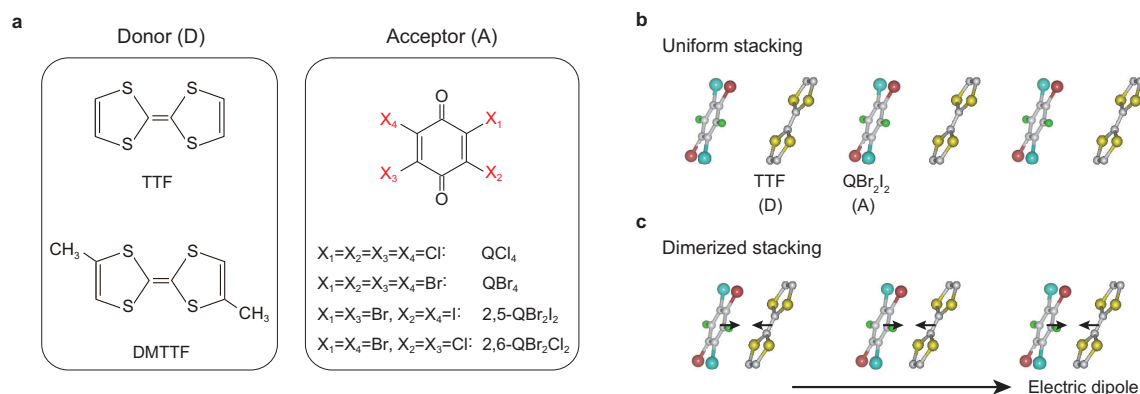

Figure 1. (**a**) Chemical forms of donor and acceptor molecules that appear in this article. (**b,c**) Schematic diagrams of the structure of the donor–acceptor mixed stack: with a uniform spacing (**b**) and in a dimerized state (**c**). Small arrows in (**c**) indicate the shifts in the molecules that occur upon dimerization.

3. Quantum Effects on Thermo-Equilibrium Properties Near the Ferroelectric QCP

In this section, focusing on TTF-2,5-QBr$_2$I$_2$, we give an overview of how quantum fluctuations that develop toward a ferroelectric QCP affect the thermo-equilibrium properties such as the ferroelectric transition temperature T_c, permittivity ϵ, and spontaneous polarization P_s.

At ambient pressure, TTF-2,5-QBr$_2$I$_2$ maintains a non-dimerized alternating stacking of TTF and 2,5-QBr$_2$I$_2$ from room temperature to the lowest temperature, and thus, the ground state is paraelectric (Figures 1b and 2a). Nevertheless, a slight enhancement of ϵ is discernible at low temperatures (Figure 2b), implying the development of dimerization fluctuations. In fact, the static dimerization of TTF and QBr$_2$I$_2$ is stabilized under moderate pressures (>0.25–0.26 GPa) (Figure 2a). In contrast to DMTTF-QCl$_4$, in which the dimerization of the donor and acceptor molecules occurs in an antiferroic manner among the neighboring stacks [22], the dimerization pattern in TTF-2,5-QBr$_2$I$_2$ under pressure is ferroic and thus gives rise to a macroscopic ferroelectric polarization oriented along the stacking direction [20].

The typical value of the ferroelectric polarization exceeds 1 μC/cm^2 in TTF-2,5-QBr$_2$I$_2$, except for at pressures very close to 0.26 GPa. Given that the dimerization transition with and without a sizable change in ionicity results in, respectively, a large value of $\approx$6.3 μC/cm^2, as in TTF-QCl$_4$ ('electronic ferroelectricity') [28], and only 0.1–0.3 μC/cm^2, as in TTF-BA ('ionic ferroelectricity') [26], the relatively large polarization above 1 μC/cm^2 in TTF-2,5-QBr$_2$I$_2$ implies that a neutral-ionic transition character or a charge degree of freedom is involved in the dimerization transition in this system as well. At the very least, in TTF-QI$_4$, which may correspond to TTF-2,5-QBr$_2$I$_2$ under negative pressure, the dimerization transition at room temperature (under $\approx$1.9 GPa) is accompanied by an increase of ionicity from 0.3 to 0.5 [33]. The difference between electronic and ionic ferroelectricity in organic charge-transfer complexes has been reviewed in [34].
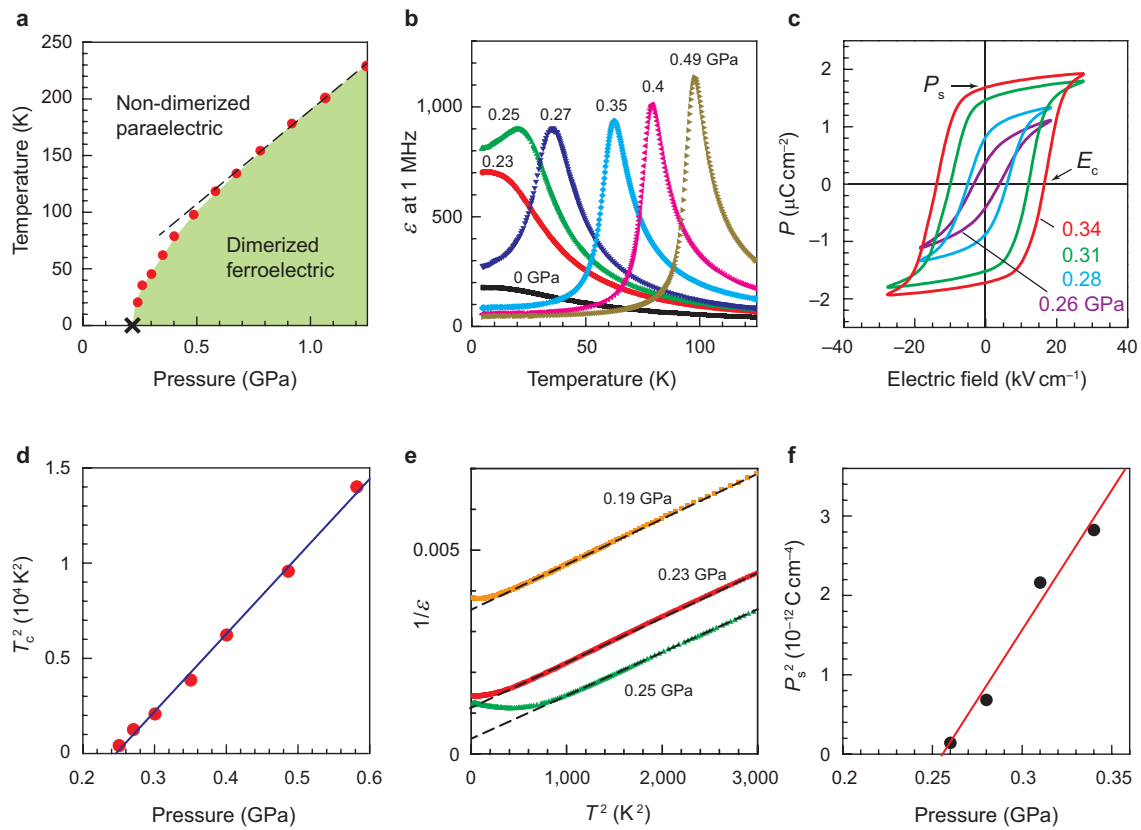
Figure 2. (**a**) Pressure–temperature phase diagram of TTF-2,5-QBr$_2$I$_2$. (**b**) Temperature dependence of the permittivity under various pressures. The applied pressure value, corrected considering its thermal change in the medium for each measurement, is represented by the value at the transition point or at the lowest temperature when the phase transition is absent. (**c**) Pressure variations in the polarization hysteresis loop measured at the lowest temperature: $T/T_c = 0.1$ for 0.28, 0.31 and 0.34 GPa, and $T/T_c = 0.3$ for 0.26 GPa. (**d**) T_c^2 versus pressure plot, highlighting the quantum critical behavior of the ferroelectric-transition temperature. The blue line represents $T_c \sim (p - p_c)^{0.5}$ with $p_c \approx 0.25$–0.26 GPa. (**e**) Inverse permittivity versus the square of the temperature. The broken lines represent $1/\epsilon \propto T^2$. (**f**) P_s^2 versus pressure plot, highlighting the quantum critical behavior of the spontaneous polarization. The red line represents $P_s \sim (p - p_c)^{0.5}$ with $p_c \approx 0.25$–0.26 GPa.

3.1. Phase Diagram

Figure 2a displays the pressure–temperature (p–T) phase diagram of TTF-2,5-QBr$_2$I$_2$, constructed based on the permittivity measurements under various pressures (Figure 2b). At pressures above 0.26 GPa, each ϵ–T profile exhibits a sharp but continuous peak at a finite temperature, indicating the presence of a ferroelectric transition (Figure 2b). The ferroelectricity is also corroborated by the observation of spontaneous polarization, P_s, below the transition temperature, T_c (Figure 2c). These observations suggest that TTF-2,5-QBr$_2$I$_2$ is a ferroelectric QCP system with pressure acting as a control parameter.

In the phase diagram, whereas T_c varies linearly with pressure in the 0.7–1.2 GPa range, the pressure dependence becomes more pronounced near the ferroelectric QCP (Figure 2a), as $T_c \sim (p - p_c)^{0.5}$ with $p_c \approx 0.25$–0.26 GPa (Figure 2d). The square-root decrease in T_c toward the ferroelectric QCP is consistent with the theoretical predictions that consider quantum-fluctuation effects [10,13,16], indicating that quantum fluctuations develop near ≈0.25–0.26 GPa.

3.2. Quantum Criticality Seen in Order-Parameter-Related Quantities

Generally, evolving quantum fluctuations are expected to significantly affect order-parameter-related quantities; for instance, permittivity and spontaneous polarization in the case of a ferroelectric transition. In fact, when the system approaches the ferroelectric QCP from high temperatures (that is, from the paraelectric phase), the inverse of the permittivity (that is, the inverse of the order-parameter susceptibility) is found to decrease as $1/\epsilon \sim T^2$ below 50 K (Figure 2e), distinct from the dependence expected for classical critical phenomena, $1/\epsilon \sim (T - T_c)$ with $T_c = 0$. Historically, the so-called Barrett formula had frequently been used to characterize an ϵ–T profile in a quantum paraelectric material located near a ferroelectric QCP [35]; however, it should be noted that the Barret formula postulates that the fluctuating order-parameter field is independent of both temperature and wavevector, an assumption incompatible with the standard phonon-softening mechanism for displacive-type ferroelectrics. By contrast, the temperature and wavevector dependence of the fluctuating order-parameter field can be incorporated, for instance, by the self-consistent-field approximation into the quantum ϕ^4-field model, and this approach leads to the theoretical prediction $1/\epsilon \propto T^2$ for a multiaxial displacive ferroelectric [14–16]. In fact, this intriguing T^2 dependence has recently been observed experimentally in the quantum ferroelectric ^{18}O substituted SrTiO$_3$ [10]. Although TTF-2,5-QBr$_2$I$_2$ possesses a strong uniaxial nature because of the donor–acceptor dimerization mechanism for the emergent ferroelectricity (Figure 1c), the theoretical prediction for multiaxial displacive ferroelectrics still appears to provide a good description of the quantum criticality regarding permittivity. This good agreement may deserve further discussion [11,12].

The quantum effect can also be identified in the spontaneous polarization (that is, the order parameter) when the system approaches the QCP from the ferroelectric phase by varying the pressure. Figure 2c displays the polarization hysteresis loop at the lowest temperatures at various pressures. Although only a limited number of data points are available, the pressure dependence of the spontaneous polarization, P_s, at the lowest temperature can be described as $P_s \sim (p - p_c)^{0.5}$ (Figure 2f), also consistent with the results of the self-consistent-field approximation to the quantum ϕ^4-field model [10,16].

Thus, the derived exponents regarding T_c, ϵ, and P_s all indicate a remarkable influence of the quantum fluctuations on the thermodynamic properties near the QCP. In addition to the ferroelectric quantum criticality, the quantum effects on the valence fluctuations that accompany the dimerization transition are also intriguing. Although this issue has not yet been explored for TTF-2,5-QBr$_2$I$_2$, quantum valence fluctuations have been detected in DMTTF-2,6-QBr$_2$Cl$_2$ at ambient pressure, which is located near an antiferroelectric QCP. In this material, the timescale of the valence fluctuations was estimated to be $\sim$30 ps by measuring the frequency shift of the infrared-active C=O stretch mode of the acceptor quinone [22]. The power-law characterizations of the quantum valence fluctuations and comparison to quantum-phase-transition theories remain to be investigated in future work.

4. Quantum Effects on the Kinetics of Ferroelectric Domain Walls Near the Ferroelectric QCP

Up to this point, we have discussed how the quantum fluctuations modify the thermodynamic properties, particularly in terms of the critical exponents. In this section, we show that quantum fluctuations also have a remarkable impact on non-equilibrium properties, such as the kinetics of ferroelectric domain walls.

Ferroelectric domain walls that separate regions with distinct electric-polarization directions are typically pinned by a pinning potential. Nevertheless, an application of a moderate electric field can induce the creep motion of domain walls with a finite probability, provided that the domain wall is under the influence of sufficient thermal fluctuations [36–45]. Conversely, as the temperature decreases, the occurrence of creep motion becomes less likely and eventually impossible under realistic electric-field magnitudes. We show here that there appears an important counter-example to this when strong quantum fluctuations are present.

4.1. Athermal Creep Motion of Domain Walls Near the QCP

Because the pattern of the dimerization dictates the direction of electric polarization, the ferroelectric domain wall in organic charge-transfer complexes is supposed to be represented by a misfit in dimerization, as schematically shown in Figure 3a [23]. When an external electric field is applied along the donor–acceptor stack, the domain with the polarization parallel to the electric field is energetically more favored, thus resulting in the shift of the domain wall at the expense of the domain with opposite polarization (Figure 3b). Because such an electric-field-induced creep motion of ferroelectric domain walls leads to an increase in the net macroscopic polarization of a specimen, measurements of permittivity enable us to probe the dynamics of the ferroelectric domain wall under a.c. electric fields, E_{ac}. Therefore, the creep motion of the ferroelectric domain walls can be addressed, for instance, by examining the non-linear effects on permittivity [46–49].
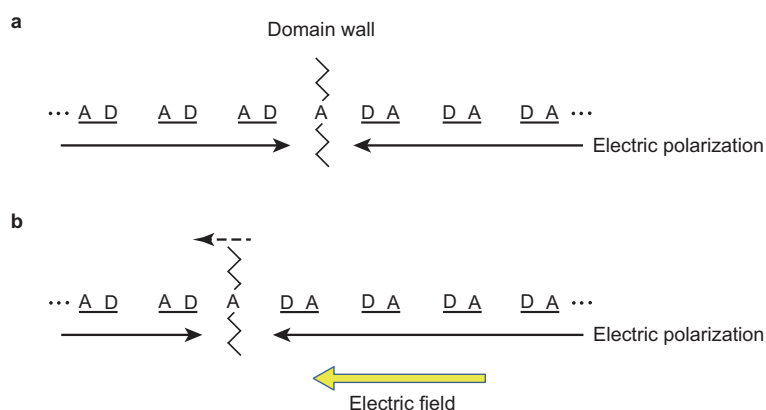

Figure 3. (**a**) Structure in the case of a head-to-head domain wall. (**b**) Shift of the domain wall under an applied electric field. TTF and 2,5-QBr$_2$I$_2$ are denoted by D (donor) and A (acceptor), respectively, and the underlines represent the dimerization of the two molecules. For simplicity, the domain wall is depicted as an atomically thin boundary, but in reality, it likely has a finite width, particularly when the system is located near the ferroelectric quantum critical point (QCP).

Figure 4a shows the temperature dependence of the permittivity at 0.34 GPa ($T_c \approx 64$ K), relatively far from the ferroelectric QCP ($p_c \approx 0.25$–0.26 GPa). We note that near T_c, the permittivity exhibits nonlinear characteristics in response to the variation in the strength of the applied E_{ac}: the ϵ measured at $E_{ac} \approx 1$ kV/cm is larger than that measured at $E_{ac} \approx 0.13$ kV/cm. Given that such a nonlinear response is characteristic of domain-wall creep [36–38], these observations indicate that the domain-wall creep makes a significant contribution to the measured permittivity, especially at $E_{ac} \approx 1$ kV/cm [39] (the analysis of the frequency–permittivity profile also leads to the same conclusion; for details, see [21]). Moreover, the nonlinear permittivity is not appreciable for $T/T_c <$ 0.6, thus indicating that the domain-wall creep at 0.34 GPa and $E_{ac} \approx 1$ kV/cm is possible only when sufficient thermal fluctuations are present. By contrast, at 0.26 GPa, which is close to p_c and hence yields a low T_c (≈ 13 K), we observe nonlinear permittivity in a broad T/T_c range, and its magnitude is approximately temperature invariant (Figure 4b), indicating the key role of quantum, rather than thermal, fluctuations.

This scenario is also supported by the temperature dependence of the coercive electric field, E_c (Figure 4c). Although E_c increases toward lower temperatures at 0.34 GPa, thus highlighting the importance of thermal fluctuations in the polarization switching process, the increase is less pronounced at lower pressures, and remarkably, E_c is nearly temperature invariant at 0.26 GPa ($\approx p_c$). Given that domain-wall creep is generally involved in the polarization reversal process, the present observations again suggest that the fluctuations facilitating the domain-wall creep are different at 0.34 and 0.26 GPa: namely, thermal and quantum fluctuations, respectively.
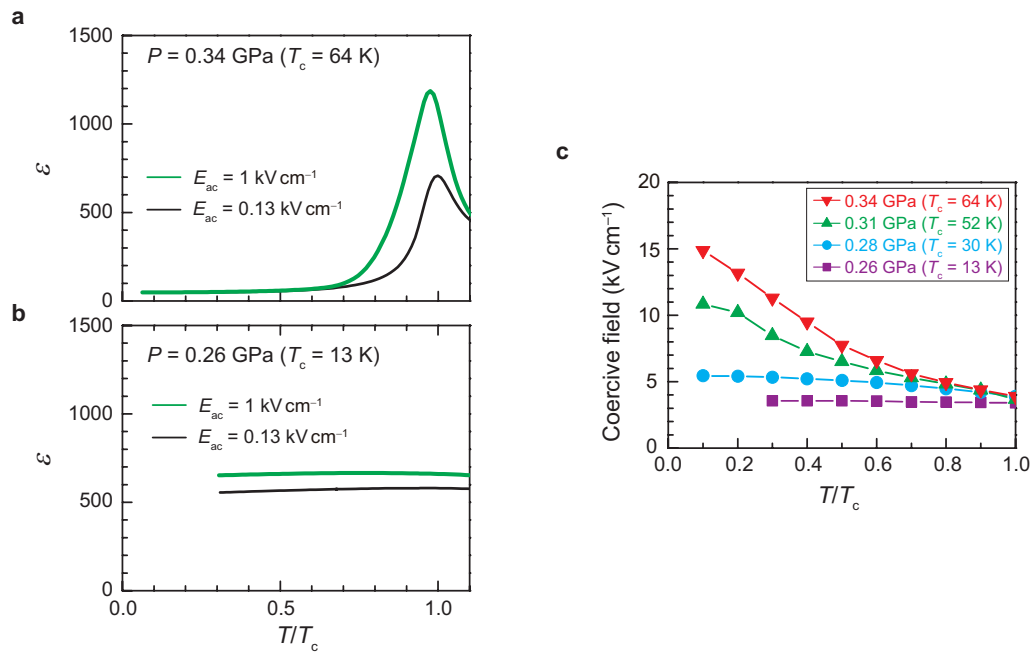
Figure 4. (**a**,**b**) Permittivity–temperature profiles measured under a.c. electric fields of different magnitudes: at 0.34 GPa ($T_c \approx 64$ K) (**a**) and at 0.26 GPa ($T_c \approx 13$ K) (**b**), the latter of which is close to the ferroelectric QCP. (**c**) Temperature dependences of the coercive electric field at different pressures. In (**a**–**c**), the temperatures are represented in the form of reduced temperatures, T/T_c.

The domain-wall creep via quantum fluctuations invokes successive quantum tunneling between adjacent minima in the multidimensional potential landscape. In the literature, quantum tunneling within an isolated double-well-potential system has been empirically deduced from the observation of the crossover behavior of the relaxation time, from the Arrhenius-type ("classical") regime at high temperatures to the temperature-invariant ('quantum') regime at low temperatures [50–52]. To extract the relaxation time associated with creep motion, we focus on the decay of the net macroscopic polarization after a poling process [53,54], a relaxation phenomenon from a single- to a multi-domain state. Because this process involves the nucleation of domains with opposite polarization and their subsequent growth via domain-wall creep, the characteristic timescale for the polarization decay is expected to be closely related to the creep dynamics.

The relaxation time associated with polarization decay can be extracted from two successive polarization hysteresis loops with the delay time of t_d, and the electric-field protocol is displayed in Figure 5a. As shown in Figure 5b, the remnant net polarization, P_r, appreciably decays with time, as observed in TTF-QCl$_4$ [28]. Figure 5c summarizes the t_d dependence of P_r at various values of T/T_c under 0.34 GPa. Dramatic prolongation of polarization retention occurs at low temperatures, and eventually, no polarization decay is seen at $T/T_c = 0.1$ on the considered time scale (1×10^{-4}–3×10^1 s), consistent with the scenario that the domain-wall creep at 0.34 GPa is facilitated by thermal fluctuations.

To extract the relaxation time τ from the decay profile, we exploit the standard relaxation equation:

$$P_r(t_d) = P_\infty + (P_0 - P_\infty) \exp\{-(t_d/\tau)^\beta\}, \tag{1}$$

where P_0 and P_∞ denote the values of P_r in the limits of $t_d \to 0$ (indicated in Figure 5b) and $t_d \to \infty$, respectively, and β is the phenomenological stretching parameter that represents the distribution of τ. We find that the polarization decay profiles yield a universal relaxation curve when $\{P_r(t_d) - P_\infty\}/(P_0 - P_\infty)$ is plotted as a function of the normalized time, t_d/τ, for each T/T_c (Figure 5d). The fitting using Equation (1) is also successful for the data at 0.31 and 0.28 GPa (not shown; for details, see ref. [21]). Remarkably, the relaxation process at 0.26 GPa is found to be nearly temperature invariant

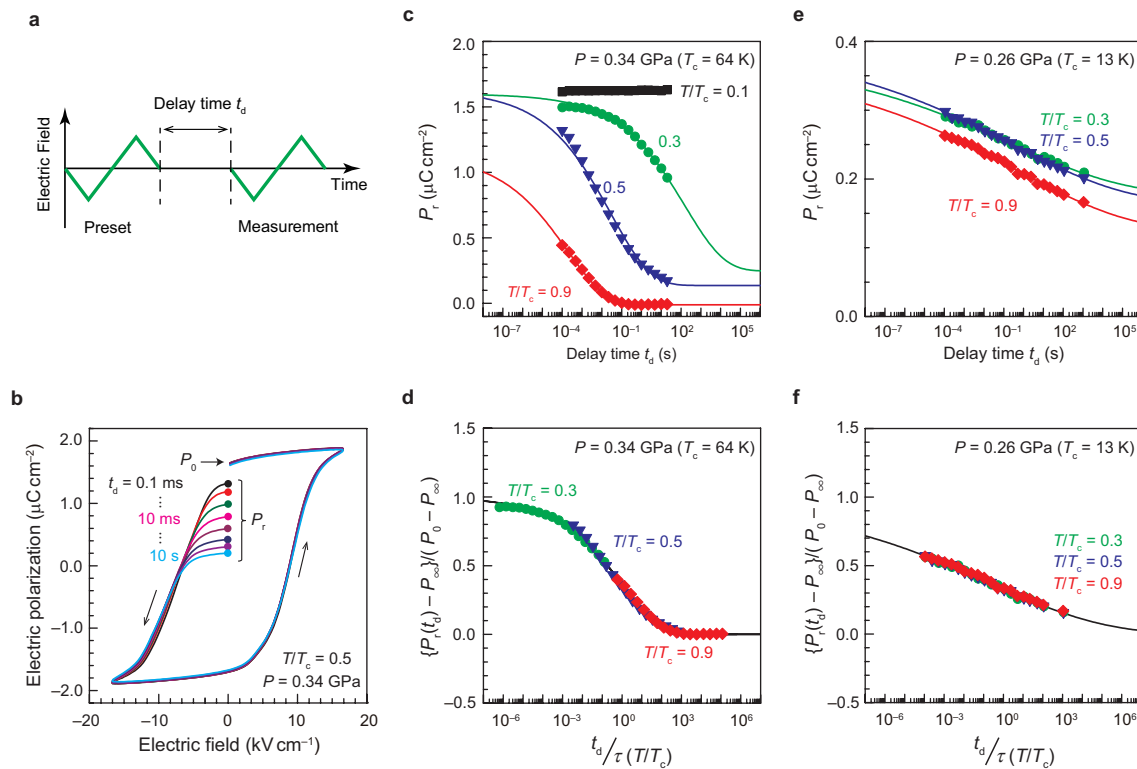(Figures 5e,f). This observation again corroborates the athermal creep motion of the domain walls at 0.26 GPa.

Figure 5. (**a**) Measurement protocol for probing the polarization decay. (**b**) Typical polarization hysteresis loops with various delay times, measured at 0.34 GPa and $T/T_c = 0.5$. (**c**) Delay-time dependences of the remnant polarization at select temperatures and 0.34 GPa ($T_c \approx 64$ K). (**d**) Normalized relaxation behavior of the polarization decay at 0.34 GPa. (**e**) Delay-time dependence of the remnant polarization at 0.26 GPa ($T_c \approx 13$ K), which is near the ferroelectric QCP. (**f**) Normalized relaxation behavior of the polarization decay at 0.26 GPa. The lines in (**c**–**f**) represent fits to the standard relaxation equation; see Equation (1).

Figure 6 summarizes the τ–$1/T$ profiles derived at various pressures. Here, three important aspects can be highlighted: first, whereas the τ–$1/T$ profile follows the thermally activated behavior or Arrhenius law at 0.34 and 0.31 GPa (a hallmark of the classical regime), a nearly temperature-invariant τ is observed at 0.26 GPa, corresponding to the behavior expected in the quantum regime; second, at the intermediate pressure of 0.28 GPa, the classical regime at high temperatures exhibits crossover behavior to the quantum regime at low temperatures; and, finally, the saturated τ value in the quantum regime, τ_{quantum}, at 0.26 GPa ($\approx p_c$) is smaller than that at 0.28 GPa. The observed classical-to-quantum crossover of τ upon approaching the QCP is consistent with the empirical evidence often used to validate quantum tunneling [50–52], indicating that the domain-wall creep near the QCP occurs exclusively via quantum tunneling between the pinning sites or metastable domain configurations (Figure 6).
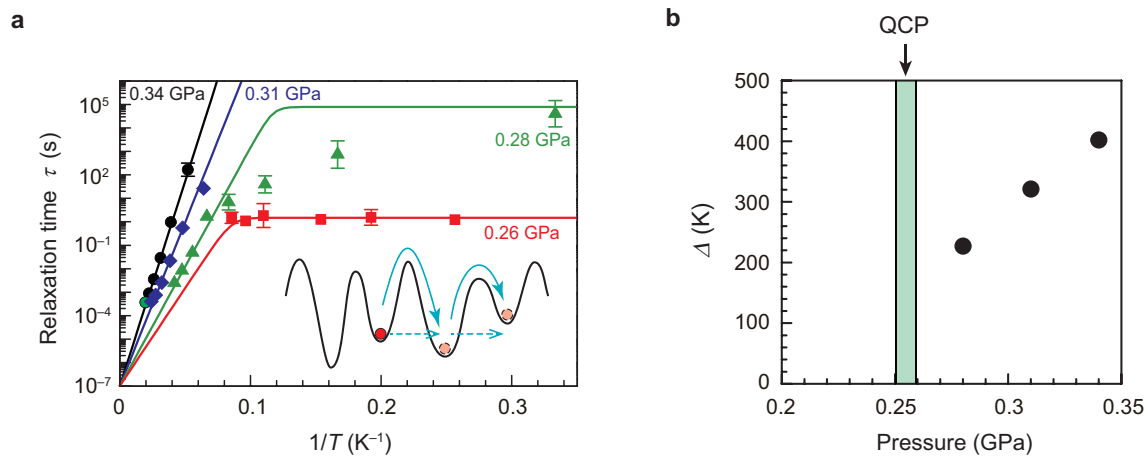
Figure 6. (**a**) Classical-quantum crossover of the ferroelectric domain-wall dynamics. The lines represent fits to Matthiessen's rule: $1/\tau = 1/\tau_{classical} + 1/\tau_{quantum}$, where $\tau_{classical}$ follows the Arrhenius law and $\tau_{quantum}$ is constant at a given pressure. The inset shows a schematic diagram comparing the classical thermally activated creep (solid arrows) with the quantum tunneling creep (broken arrows) of a domain wall (modeled as a particle). The multi-valley schematic represents a multidimensional potential landscape. (**b**) Pressure dependence of Δ, derived from (**a**).

4.2. Effective Mass of the Ferroelectric Domain Wall Near the QCP

Having observed the classical-quantum crossover regarding the creep motion, the effective mass of the ferroelectric domain wall, m_{eff}, can be estimated, at least within the framework of the simplest Wentzel–Kramers–Brillouin (WKB) approximation [51,52]:

$$\tau_{quantum} = \tau_0 \exp(2w\sqrt{2m_{eff}\Delta/\hbar^2}), \tag{2}$$

where w is the domain-wall tunneling distance [where we adopt a value of $\approx$7.29 Å (6.5 K, 0.2 GPa) as the unit-cell length along the stacking direction]; $2\pi\tau_0$ and Δ represent the inverse of the attempt frequency and the activation barrier, respectively, and both quantities appear in the Arrhenius behavior, $\tau_{classical} = \tau_0\exp(-\Delta/k_BT)$, that is used to characterize the classical regime. In the fitting, τ_0 is assumed to be pressure invariant in the considered pressure range and can be graphically estimated to be $\approx$10^{-7}s from Figure 6a as the τ value at $1/T = 0$. In the calculation of m_{eff}, we focus on the data at 0.28 GPa because the values of both $\tau_{quantum}$ and Δ can be extracted at the same pressure; then, the order of magnitude of m_{eff} at 0.28 GPa is estimated to be $\approx$5$\times$10^2 m_e (m_e denotes the electron mass).

Given that the proton, which is anticipated to be capable of quantum tunneling in matter [55,56], has a mass of $\approx$1.8 $\times$ 10^3 m_e, the estimated m_{eff} is reasonably small. Here, it should be noted that even though the domain-wall creep entails the displacement of TTF and QBr$_2$I$_2$ molecules (Figure 3b), m_{eff} is much smaller than the masses of the TTF and QBr$_2$I$_2$ molecules ($\approx$3.7 $\times$ 10^5 and $\approx$9.4 $\times$ 10^5 m_e, respectively). While this result may appear counterintuitive, a similar situation is also observed in polyacetylene, where the mass of the building blocks (carbon atoms) is $\approx$2.2 $\times$ 10^4 m_e, whereas the m_{eff} of the bond soliton (or, equivalently, the misfit in the C=C paring) is only $\approx$10 m_e (ref. [57]). Given that the small m_{eff} of the bond soliton in polyacetylene has been rationalized in terms of a large soliton width of $\approx$14 unit cells [58], it can be expected that the domain-wall width in TTF-QBr$_2$I$_2$ becomes increasingly broadened as the system approaches the ferroelectric QCP; in fact, although the amount of quenched randomness is supposed to be unchanged with pressure variations, Δ decreases toward the ferroelectric QCP (Figure 6b), suggesting an increase in the domain-wall width. We expect that such a broadened domain-wall width gives rise to the unexpectedly small effective mass and thus the quantum-particle nature of the domain wall.

5. Conclusions

We have reviewed the findings that TTF-2,5-QBr$_2$I$_2$ exhibits a ferroelectric QCP at a moderate pressure ($p_c \approx 0.25$–0.26 GPa), thus allowing the study of ferroelectric quantum criticality. The effects of the enhanced quantum criticality are manifested both in the thermodynamic properties, such as T_c, ϵ, and P_s, and in the non-equilibrium properties, such as the ferroelectric domain-wall creep motion under electric fields. In particular, the temperature-independent nature of the domain-wall creep suggests that the domain walls can move even at the lowest temperature with the help of quantum fluctuations.

One of the advantages of a pressure-tunable quantum ferroelectric material is that the amount of quenched disorder is preserved throughout the systematic studies, unlike in the case where chemical doping is used as a control parameter. Besides the fact that molecular solids are generally sensitive to pressure, the neutral-ionic-instability that is involved in many organic-charge transfer complexes may further increase the sensitivity to pressure. Therefore, organic ferroelectrics consisting of a donor–acceptor mixed stack provide a unique platform for the study of ferroelectric quantum criticality.

Conflicts of Interest: The authors declare no conflict of interest. The founding sponsors had no role in the design of the study; in the collection, analyses, or interpretation of data; in the writing of the manuscript, and in the decision to publish the results.

References

1.　Sachdev, S. *Quantum Phase Transitions*; Cambridge Univ. Press: Cambridge, UK, 1999.
2.　Coleman, P.; Schofield, A.J. Quantum criticality. *Nature* **2005**, *433*, 226–229.
3.　Sachdev, S. Quantum criticality in heavy-fermion metals. *Nat. Phys.* **2008**, *4*, 173–185.
4.　Gegenwart, P.; Si, Q.; Steglich, F. Quantum criticality in heavy-fermion metals. *Nat. Phys.* **2008**, *4*, 186–197.
5.　Löhneysen, H.V.; Pietrus, T.; Portisch, G.; Schlager, H.G.; Schröder, A.; Sieck, M.; Trappmann, T. Non-Fermi-liquid behavior in a heavy-fermion alloy at a magnetic instability. *Phys. Rev. Lett.* **1994**, *72*, 3262–3265.
6.　Custers, J.; Gegenwart, P.; Wilhelm, H.; Neumaier, K.; Tokiwa, Y.; Trovarelli, O.; Geibel, C.; Steglich, F.; Pépin, C.; Coleman, P. The break-up of heavy electrons at a quantum critical point. *Nature* **2003**, *424*, 524–527.
7.　Mathur, N.D.; Grosche, F.M.; Julian, S.R.; Walker, I.R.; Freye, D.M.; Haselwimmer, R.K.W.; Lonzarich, G.G. Magnetically mediated superconductivity in heavy fermion compounds. *Nature* **1998**, *394*, 39–43.
8.　Park, T.; Ronning, F.; Yuan, H.Q.; Salamon, M.B.; Movshovich, R.; Sarrao, J.L.; Thompson, J.D. Hidden magnetism and quantum criticality in the heavy fermion superconductor CeRhIn$_5$. *Nature* **2006**, *440*, 65–68.
9.　Löhneysen, H.V.; Rosch, A.; Vojta, M.; Wölfle, P. Fermi-liquid instabilities at magnetic quantum phase transitions. *Rev. Mod. Phys.* **2007**, *79*, 1015–1075.
10.　Rowley, S.E.; Spalek, L.J.; Smith, R.P.; Dean, M.P.M.; Itoh, M.; Scott, J.F.; Lonzarich, G.G.; Saxena, S.S. Ferroelectric quantum criticality. *Nat. Phys.* **2014**, *10*, 367–372.
11.　Rowley, S.E.; Hadjimichael, M.; Ali, M.N.; Durmaz, Y.C.; Lashley, J.C.; Cava, R.J.; Scott, J.F. Quantum Criticality in a uniaxial organic ferroelectric. *J. Phys. Condens. Matter* **2015**, *27*, 395901.
12.　Rowley, S.E.; Chai, Y.-S.; Shen, S.-P.; Sun, Y.; Jones, A.T.; Watts, B.E.; Scott, J.F. Uniaxial ferroelectric quantum criticality in multiferroic hexaferrites BaFe$_{12}$O$_{19}$ and SrFe$_{12}$O$_{19}$. *Sci. Rep.* **2016**, *6*, 25724.
13.　Morf, R.; Scheider, T.; Stoll, E. Nonuniversal critical behavior and its suppression by quantum fluctuations. *Phys. Rev. B* **1977**, *16*, 462–469.
14.　Roussev, R.; Millis, A.J. Theory of the quantum paraelectric-ferroelectric transition. *Phys. Rev. B* **2003**, *67*, 014105.
15.　Das, N.; Mishra, S.G. Fluctuations and criticality in quantum paraelectrics. *J. Phys. Condens. Matter* **2009**, *21*, 095901.
16.　Pálová, L.; Chandra, P.; Coleman, P. Quantum critical paraelectrics and the Casimir effect in time. *Phys. Rev. B* **2009**, *79*, 075101.

17. Belitz, D.; Kirkpatrick, T.R.; Vojta, T. How generic scale invariance influences quantum and classical phase transitions. *Rev. Mod. Phys.* **2005**, *77*, 579–632.

18. Grigera, S.A.; Gegenwart, P.; Borzi, R.A.; Weickert, F.; Schofield, A.J.; Perry, R.S.; Tayama, T.; Sakakibara, T.; Maeno, Y.; Green, A.G.; Mackenzie, A.P. Disorder-Sensitive Phase Formation Linked to Metamagnetic Quantum Criticality. *Science* **2004**, *306*, 1154–1157.

19. Lester, C.; Ramos, S.; Perry, R.S.; Croft, T.P.; Bewley. R.I.; Guidi, T.; Manuel, P.; Khalyavin, D.D.; Forgan, E.M.; Hayden, S.M. Field-tunable spin-density-wave phases in $Sr_3Ru_2O_7$. *Nat. Mat.* **2015**, *14*, 373–378.

20. Horiuchi, S.; Kobayashi, K.; Kumai, R.; Minami, N.; Kagawa, F.; Tokura, Y. Quantum ferroelectricity in charge-transfer complex crystals. *Nat. Commun.* **2016**, *6*, 16075.

21. Kagawa, F.; Minami, N.; Horiuchi, S.; Tokura, Y. Athermal domain-wall creep near a ferroelectric quantum critical point. *Nat. Commun.* **2015**, *6*, 7469.

22. Horiuchi, S.; Okimoto, Y.; Kumai, R.; Tokura, Y. Quantum Phase Transition in Organic Charge-Transfer Complexes. *Science* **2003**, *299*, 229–232.

23. Nagaosa, N. Theory of Neutral-Ionic Transition in Organic Crystals. III. Effec of the Electron-Lattice Interaction. *J. Phys. Soc. Jpn.* **1986**, *55*, 2754–2764.

24. Soos, Z.G.; Bewick, S.A.; Peri, A.; Painelli, A. Dielectric response of modified Hubbard models with neutral-ionic and Peierls transitions. *J. Chem. Phys.* **2004**, *120*, 6712–6720.

25. Soos, Z.G.; Painelli, A. Metastable domains and potential energy surfaces in organic charge-transfer salts with neutral-ionic phase transitions. *Phys. Rev. B* **2007**, *75*, 155119.

26. Kagawa, F.; Horiuchi, S.; Tokunaga, M.; Fujioka, J.; Tokura, Y. Ferroelectricity in a one-dimensional organic quantum magnet. *Nat. Phys.* **2010**, *6*, 169–172.

27. Torrance, J.B.; Girlando, A.; Mayerle, J.J.; Crowley, J.I.; Lee, V.Y.; Batail, P.; LaPlaca, S.J. Anomalous Nature of Neutral-to-Ionic Phase Transition in Tetrathiafulvalene-Chloranil. *Phys. Rev. Lett.* **1981**, *47*, 1747–1750.

28. Kobayashi, K.; Horiuchi, S.; Kumai, R.; Kagawa, F.; Murakami, Y.; Tokura, Y. Electronic Ferroelectricity in a Molecular Crystal with Large Polarization Directing Antiparallel to Ionic Displacement. *Phys. Rev. Lett.* **2012**, *108*, 237601.

29. Girlando, A.; Pecile, C.; Torrance, J.B. A key to understanding ionic mixed stacked organic-solids—Tetrathiafulvalene-bromanil (TTF-BA). *Solid State Commun.* **1985**, *54*, 753–759.

30. García, P.; Dahaoui, S.; Fertey, P.; Wenger, E.; Lecomte, C. Crystallographic investigation of temperature-induced phase transition of the tetrathiafulvalene-*p*-bromanil, TTF-BA charge transfer complex. *Phys. Rev. B* **2005**, *72*, 104115.

31. Lemée-Cailleau, M.H.; Le Cointe, M.; Cailleau, H.; Luty, T.; Moussa, F.; Roos, J.; Brinkmann, D.; Toudic, B.; Ayache, C.; Karl, N. Thermodynamics of the Neutral-to-Ionic Transition as Condensation and Crystallization of Charge-Transfer Excitations. *Phys. Rev. Lett.* **1997**, *79*, 1690–1693.

32. Sadohara, R.; Matsuzaki, S. Neutral-ionic transition of charge transfer complexes of TTF and tetrahalo-*p*-benzoquinones. *Mol. Cryst. Liq. Cryst.* **1997**, *296*, 269–280.

33. Matsuzaki, S.; Hiejima, T.; Sano, M. Pressure-induced neutral-ionic phase transition of a tetrathiafulvalene-iodanil crystal. *Bull. Chem. Soc. Jpn.* **1991**, *64*, 2052–2057.

34. Horiuchi, S.; Kobayashi, K.; Kumai, R.; Ishibashi, S. Ionic versus Electronic Ferroelectricity in Donor-Acceptro Molecular Sequences. *Chem. Lett.* **2014**, *43*, 26–35.

35. Barrett, J.H. Dielectric constant in perovskite type crystals. *Phys. Rev.* **1952**, *86*, 118–120.

36. Miller, R.C.; Savage, A. Velocity of Sidewise 180 Domain-Wall Motion in $BaTiO_3$ as a Function of Applied Electric Field. *Phys. Rev.* **1958**, *112*, 755–762.

37. Tybell, T.; Paruch, P.; Giamarchi, T.; Triscone, J.-M. Domain Wall Creep in Epitaxial Ferroelectric $Pb(Zr_{0.2}Ti_{0.8})O_3$ Thin Films. *Phys. Rev. Lett.* **2002**, *89*, 097601.

38. Jo, J.Y.; Yang, S.M.; Kim, T.H.; Lee, H.N.; Yoon, J.-G.; Park, S.; Jo, Y.; Jung, M.H.; Noh, T.W. Nonlinear Dynamics of Domain-Wall Propagation in Epitaxial Ferroelectric Thin Films. *Phys. Rev. Lett.* **2009**, *102*, 045701.

39. Wang, Y.L.; Tagantsev, A.K.; Damjanovic, D.; Setter, N. Giant domain wall contribution to the dielectric susceptibility in $BaTiO_3$ single crystals. *Appl. Phys. Lett.* **2007**, *91*, 062905.

40. Shur, V.Y.; Rumyantsev, E.L.; Nikolaeva, E.V.; Shishkin, E.I. Formation and evolution of charged domain walls in congruent lithium niobate. *Appl. Phys. Lett.* **2000**, *77*, 3636–3638.

41. Balke, N.; Gajek, H.; Tagantsev, S.K.; Martin, L.W.; Chu, Y.-H.; Ramesh, R.; Kalinin, S.V. Direct Observation of Capacitor Switching Using Planar Electrodes. *Adv. Funct. Mater.* **2010**, *20*, 3466–3475.

42. Kagawa, F.; Horiuchi, S.; Minami, N.; Ishibashi, S.; Kobayashi, K.; Kumai, R.; Murakami, Y.; Tokura, Y. Polarization Switching Ability Dependent on Multidomain Topology in a Uniaxial Organic Ferroelectric. *Nano Lett.* **2014**, *14*, 239–243.

43. Chauve, P.; Giamarchi, T.; Le Doussal, P. Creep and depinning in disordered media. *Phys. Rev. B* **2000**, *62*, 6241–6267.

44. Shin, Y.-H.; Grinberg, I.; Chen, I.-W.; Rappe, A.M. Nucleation and growth mechanism of ferroelectric domain-wall motion. *Nature* **2007**, *449*, 881–884.

45. Kolton, A.B.; Rosso, A.; Giamarchi, T.; Krauth, W. Creep dynamics of elastic manifolds via exact transition pathways. *Phys. Rev. B* **2009**, *79*, 184207.

46. Kleemann, W. Universal Domain Wall Dynamics in Disordered Ferroic Materials. *Annu. Rev. Mater. Res.* **2007**, *37*, 415–448.

47. Braun, T.; Kleemann, W.; Dec, J.; Thomas, P.A. Creep and Relaxation Dynamics of Domain Walls in Periodically Poled KTiOPO$_4$. *Phys. Rev. Lett.* **2005**, *94*, 117601.

48. Kagawa, F.; Horiuchi, S.; Matsui, H.; Kumai, R.; Onose, Y.; Hasegawa, T.; Tokura, Y. Electric-Field Control of Solitons in a Ferroelectric Organic Charge-Transfer Salt. *Phys. Rev. Lett.* **2010**, *104*, 227602.

49. Kagawa, F.; Hatahara, K.; Horiuchi, S.; Tokura, Y. Domain-wall dynamics coupled to proton motion in a hydrogen-bonded organic ferroelectric. *Phys. Rev. B* **2012**, *85*, 220101.

50. Hemberger, J.; Lunkenheimer, P.; Viana, R.; Böhmer, R.; Loidl, A. Electric-field-dependent dielectric constant and nonlinear susceptibility in SrTiO$_3$. *Phys. Rev. B* **1995**, *52*, 13159–13162.

51. Brooke, J.; Rosenbaum, T.F.; Aeppli, G. Tunable quantum tunneling of magnetic domain walls. *Nature* **2001**, *413*, 610–613.

52. Shpyrko, O.G.; Isaacs, E.D.; Logan, J.M.; Feng, Y.; Aeppli, G.; Jaramillo, R.; Kim, H.C.; Rosenbaum, T.F.; Zschack, P.; Sprung, M.; Narayanan, S.; Sandy, A.R. Direct measurement of antiferromagnetic domain fluctuations. *Nature* **2007**, *447*, 68–71.

53. Mehta, R.R.; Silverman, B.D.; Jacobs, J.T. Depolarization fields in thin ferroelectric films. *J. Appl. Phys.* **1973**, *44*, 3379–3385.

54. Benedetto, J.M.; Moore, R.A.; McLean, F.B. Effects of operating conditions on the fast-decay component of the retained polarization in lead zirconate titanate thin films. *J. Appl. Phys.* **1994**, *75*, 460–466.

55. Clemens, J.M.; Hochstrasser, R.M.; Trommsdorff, H.P. Direct studies of proton tunneling in hydrogen bonded mixed molecular crystals by optical excitation. *J. Chem. Phys.* **1984**, *80*, 1744–1753.

56. Neumann, M.; Brougham, D.F.; McGloin, C.J.; Johnson, M.R.; Horsewill, A.J.; Trommsdorff, H.P. Proton tunneling in benzoic acid crystals at intermediate temperatures: Nuclear magnetic resonance and neutron scattering studies. *J. Chem. Phys.* **1998**, *109*, 7300–7311.

57. Champagne, B.; Deumens, E.; Öhrn, Y. Vibrations and soliton dynamics of positively charged polyacetylene chains. *J. Chem. Phys.* **1997**, *107*, 5433–5444.

58. Heeger, A.J.; Kivelson, S.; Schrieffer, J.R.; Su, W.-P. Solitons in conducting polymers. *Rev. Mod. Phys.* **1988**, *60*, 781–850.